

Upper-bound and finite element analyses of multi-row sprocket during cold semi-precision forging process

Wangjun Cheng^{1,2} · Chengzhong Chi² · Yongzhen Wang² · Peng Lin² · Wei Liang²

Received: 25 January 2015 / Revised: 2 June 2015 / Accepted: 5 June 2015 / Published online: 2 August 2015
© The Author(s) 2015. This article is published with open access at Springerlink.com

Abstract The cold semi-precision forging of a multi-row sprocket was investigated using upper-bound (UB) and finite element methods combined with experiments. Based on the design of a new tooth profile for the sprocket, a cold semi-precision forging process and a kinematically admissible velocity field for filling the die cavity were proposed. Using the UB method, the velocity fields of the sprocket billet in the forming process were divided theoretically and calculated. The process of forging a multi-row sprocket was simulated using the FEM package Deform-3D V6.1 to obtain the distributions of the velocity field and the effective stress field in filling the die cavity. Similar to the simulated results, the experiment on cold forging a 5052 aluminum alloy sprocket was successfully performed. By comparing the calculated (UB method), experimental and simulated load-stroke curves, the calculated and simulated results were basically in accordance with the experimental results. The study provides a theoretical foundation for the development of the precision forging of multi-row sprockets.

Keywords Multi-row sprocket · Cold semi-precision forging · Upper-bound method · Finite element analysis

1 Introduction

A multi-row sprocket is a complicated part widely used in chain driving systems for mining machinery and equipment, such as scraper conveyers. The tooth profiles of multi-row sprockets are conventionally machined using a hobbing process, which wastes material and lowers their strength. Common failures of sprockets in the complex environment of a coal mine are excessive wears and tooth fractures (Wang et al. 2012). The chain and multi-row sprockets often bear larger static and dynamic loads in the impact-fluctuating work conditions of a scraper conveyer (Jiao et al. 2014). Therefore, improving the strength of multi-row sprocket plays an extremely important role in the

driving system of mining equipment. Thipprakmas (2011) presented the fine-blanking process for manufacturing sprockets improving their strength with simple processing operations, reducing production time and costs. Takagi et al. (2009) used the technology of powder metallurgy to compact the housing sprocket while maintaining dimensional tolerances and strength. As a whole, the precision forging of multi-row sprockets is a complex process with severe plastic deformation (SPD) which improves the mechanical properties of forged parts.

In recent years, many researchers have reported the analysis process of forging gears using the upper-bound method and finite element method, but no attempt has been made to analyze the precision forging of multi-row sprockets. Upper-bound and FE methods are characterized by less computation time and reasonable accuracy (Can and Misirli 2008). Choi et al. (2000) proposed a mathematical method using the upper-bound method to forge a spur gear from a hollow billet. Choi and Choi (1998) also modeled a new tooth profile to obtain a more practical method to analyze the kinematically admissible velocity fields in external spur gear forging. Politis et al. (2014)

✉ Wangjun Cheng
chengwangjun2008@126.com

¹ China National Heavy Machinery Research Institute Co., Ltd., Xi'an 710032, China

² College of Materials Science and Engineering, Taiyuan University of Technology, Taiyuan 030024, China

established a simplified FE model to obtain the material flow behaviors and thickness distributions of forged Bi-metal gears. Compared with analyzing spur gear forging using the upper-bound and finite element methods above, the cold semi-precision forging with upper-bound and finite element methods for multi-row sprockets is a new approach to establishing similarity in the tooth profiles of the gear and sprocket.

This study aims to analyze the velocity fields of a multi-row sprocket billet based on the upper-bound method. The effective stress fields were investigated using the FEM software DEFORM-3D V6.1. The new forming processes were verified by experiments using aluminum alloy. The flow-ability of material, filling-quality of the dies and load-stroke curves were respectively obtained during the cold semi-precision forging of a multi-row sprocket. It is expected that this study will provide meaningful guidance in assessing the design of the die and determining the manufacturing process of multi-row sprockets.

2 Cold forging process

A multi-row sprocket possesses a complex structure, with three rows of tooth profiles on the circumference of cylindrical surface and two groups of flange grooves in the tooth profiles. A diagram of a multi-row sprocket part is shown in Fig. 1. The tooth profile is the main forming part in forging it. Currently, it is generally machined using a hobbing process to form the teeth. The cold precision forging processes of a multi-row sprocket are still in the experimental stage because of the complicated processing conditions. In this study, based on the modified sprocket forging profiles (Zhao et al. 2014), a new forging process is presented for the cold semi-precision forging of a multi-row sprocket. The order of processing is shown in Fig. 2.

3 Upper-bound analysis

3.1 Velocity fields assumption

A new simple type of sprocket tooth profile (Fig. 3) was designed to reduce the stress concentrations and cracks in the die cavity in cold semi-precision forging. The cylindrical coordinate (r, θ, z) system was used to analyze the velocity fields of the billet for the multi-row sprocket. The present theories were employed based on the upper-bound method with the following assumptions: (1) The friction coefficient is a constant value in the contact surface between the die and billet. (2) The material is perfectly rigid plastic, homogeneous and obeys Von Mises's yield criterion. (3) The billet volume remains constant in die

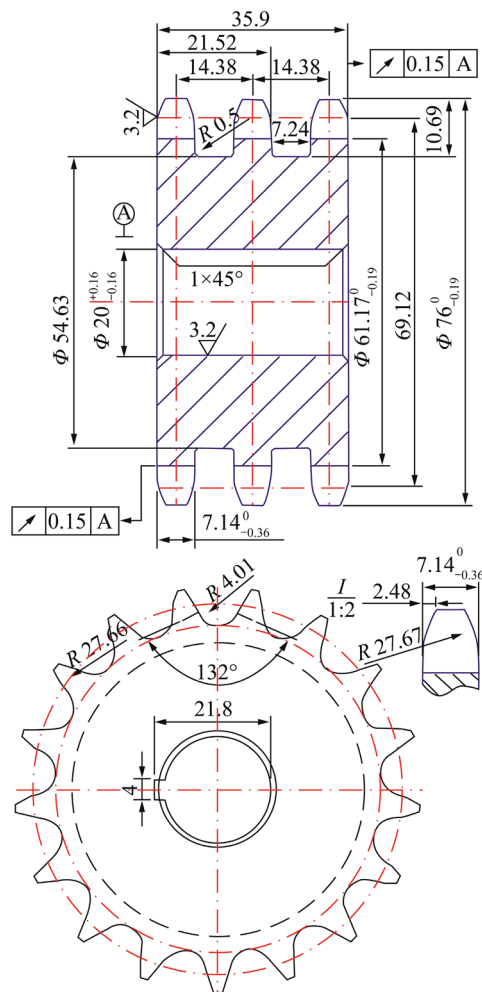


Fig. 1 Diagram of a multi-row sprocket part (unit: mm)



Fig. 2 Order of processing a multi-row sprocket

cavity filling. (4) The billet filling is continuous without overlaps and cracks. (5) The external diameter of the hollow billet is equal to the root circle of the multi-sprocket.

3.2 Dividing deformation regions

There is a flow diversion surface with zero speed in forming the cylindrical hollow billet process, in which the material flows inwards inside the radius of the shunt circle and outwards outside the shunt circle (Ghassemali et al. 2013; Wu et al. 2014). The outside diameter of the hollow billet is smaller than the root circle of the multi-sprocket. Therefore, the upsetting process in initially filling the die

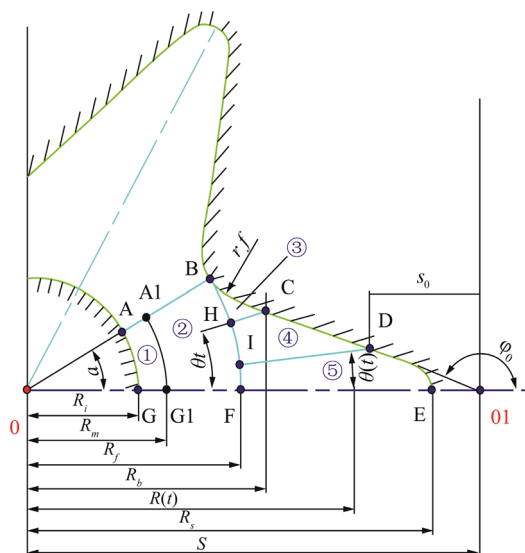


Fig. 3 Divided deformation regions for the cold forging of a sprocket

cavity was ignored to facilitate analysis (Wu and Wang 1992; Yang et al. 1999). The multi-row sprocket billet was divided into $2N$ deformation units and each unit ($N/2$) was subdivided into five plastic deformation zones whose boundaries were ABCDEFGHI. It was assumed that billet fluids cannot cross or shear along the symmetrical planes AB and EFG. Hence half a tooth is used to analyze deformation characteristics throughout the cold semi-precision forging process.

3.3 Kinematically admissible velocity

The velocity of the billet should satisfy the boundary conditions, the parallel velocity field assumptions and volume constancy, expressed as below:

$$\dot{\epsilon}_{RR} = \frac{\partial U_R}{\partial R}, \quad \dot{\epsilon}_{\theta\theta} = \frac{1}{R} \left(\frac{\partial U_\theta}{\partial \theta} + U_R \right), \quad \dot{\epsilon}_{zz} = \frac{\partial U_z}{\partial z}, \quad (1)$$

$$\dot{\epsilon}_v = \dot{\epsilon}_{RR} + \dot{\epsilon}_{\theta\theta} + \dot{\epsilon}_{zz} = 0.$$

Assuming the upper die moves down with unit flow velocity u , the axial velocity U_z and the axial strain rate $\dot{\epsilon}_{zz}$ were given as:

$$U_z = -\frac{u}{t}z, \quad \dot{\epsilon}_{zz} = -\frac{u}{t}. \quad (2)$$

3.3.1 Deformation region ① ($0 \leq \theta \leq \alpha, R_i \leq R \leq R_m$)

The radial velocity U_R was zero because of the constraint on the central mandrel surface AG and the excess metal flowed into region ② across the boundary A1G1. The circumferential velocity U_θ was calculated assuming a constant volume. The velocity field and strain rates for this region were calculated as follows:

$$U_R = 0, \quad U_\theta = \frac{u\theta R}{t}, \quad \dot{\epsilon}_{RR} = 0, \quad \dot{\epsilon}_{\theta\theta} = -\frac{u}{t}. \quad (3)$$

3.3.2 Deformation region ② ($0 \leq \theta \leq \alpha, R_m \leq R \leq R_f$)

The excess metal in region ① flowed into region ② across the boundary A1G1 and then into region ③④⑤ through the boundary BHIF. Therefore, boundaries A1G1 and BHIF satisfied the continuous conditions of deformation. The radial velocity U_R in the boundary A1G1 and the circumferential velocity U_θ along the symmetric line were zero (Kwan 2002). The velocity distribution and the strain rates in this region were calculated as:

$$U_\theta = \frac{u\theta R a - \theta}{t \alpha}, \quad (4)$$

$$U_R = \frac{u}{2t} \left(R - \frac{R_m^2}{R} \right). \quad (5)$$

Hence if $\theta = \alpha$, the calculated results were shown as follows:

$$U_\theta = 0, \quad \dot{\epsilon}_{\theta\theta} = \frac{U_R}{R}, \quad (6)$$

$$U_R = \frac{u}{2t} \left(R - \frac{R_m^2}{R} \right), \quad (7)$$

$$\dot{\epsilon}_{RR} = \frac{\partial U_R}{\partial R} = \frac{u}{2t} \left(1 + \frac{R_m^2}{R^2} \right). \quad (8)$$

3.3.3 Deformation region ③ ($\theta_f \leq \theta \leq \alpha, R_f \leq R \leq R_b$)

Assuming the fillet radius of the tooth groove circle for the sprocket is r_f , the velocity field in this region was assumed as follows:

$$U_R = \frac{uR}{2t} + \frac{c_1}{R}, \quad (9)$$

$$U_\theta = \left(\frac{uR}{2t} + \frac{c_1}{R} \right) \cot \varphi, \quad (10)$$

$$c_1 = \frac{uR_f^2}{2t} \left(\frac{\theta_f}{\alpha - \theta_f} \right) + \frac{uR_m^2}{2t} \left(\frac{\alpha}{\alpha - \theta_f} \right), \quad (11)$$

$$\dot{\epsilon}_{RR} = \frac{\partial U_R}{\partial R} = \frac{u}{2t} - \frac{c_1}{R^2}, \quad (12)$$

$$\dot{\epsilon}_{\theta\theta} = \frac{1}{R} \left(\frac{\partial U_\theta}{\partial \theta} + U_R \right) = \frac{u}{2t} + \frac{c_1}{R^2}, \quad (13)$$

where $\cot \varphi$ is a cotangent function associated with r_f, R_f , and R .

3.3.4 Deformation region ④ ($\theta_d \leq \theta \leq \theta_f, R_b \leq R \leq R(t)$)

To simplify the complicated relations, the translational coordinate system (Fig. 4) was constructed placing the

point O_1 as a new coordinate origin. The tangential flow of metal in the deformation zone ④ was bound by molding of the inner surface CD, which satisfied the continuous condition between boundary CH and HI. If $\varphi = \varphi_0$ or $\varphi = \pi$, the circumferential velocity U_θ was assumed to be zero. Thus the velocity and strain rate fields are given by:

$$U_\varphi = c_1\rho(\varphi - \varphi_0)(\varphi - \pi), \tag{14}$$

$$U_\rho = \left(\frac{\rho}{2} + \frac{c_3}{c_2\rho}\right) \left[\frac{u}{t} - c_1(2\varphi - \pi - \varphi_0)\right], \tag{15}$$

$$\dot{\epsilon}_{\varphi\varphi} = \frac{1}{\rho} [c_1\rho(2\varphi - \pi - \varphi_0) + U_\rho], \tag{16}$$

$$\dot{\epsilon}_{\rho\rho} = \frac{\rho^2 - 2}{2\rho^2} \left[\frac{u}{t} - c_1(2\varphi - \pi - \varphi_0)\right], \tag{17}$$

where c_1, c_2, c_3 represent the undetermined constants. The relationship between θ and φ can be characterized by the following equations:

$$r \sin \theta = \rho \sin(\pi - \varphi), \tag{18}$$

$$\rho^2 + s^2 - 2\rho s \cos(\pi - \varphi) = r^2. \tag{19}$$

The velocity condition of the boundary HI was obtained from:

$$U_\rho \cos(\theta - \varphi) + U_\varphi \sin(\theta - \varphi) = \frac{u}{2t} \left(r - \frac{r_m^2}{r}\right). \tag{20}$$

3.3.5 Deformation region ⑤ ($0 \leq \theta \leq \theta_d, R_f \leq R \leq R_s$)

Because of the constraint of boundary DE, the radial velocity approximated to zero when billet fluids filled the die cavity. The excess metal in region ④ flowed into region ⑤ across the boundary ID, which satisfied the continuous condition on the boundary ID. It was observed that the width of the sprocket teeth was too small. Therefore, when p was equal to s_0 , it was concluded that the radial velocity was approximately zero. The velocity field and strain rate respectively come out to be:

$$U_\varphi = (\varphi - \pi) \left[\rho \left(\frac{u}{t} + 2d_1\right) - d_1s_0\right], \tag{21}$$

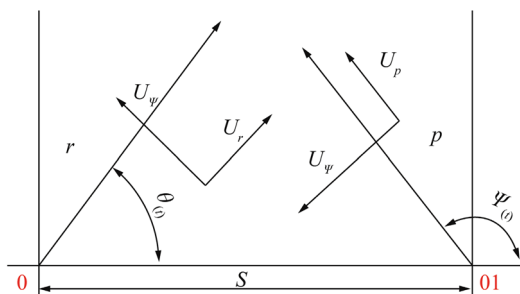


Fig. 4 Coordinates transformation diagram

$$U_\rho = d_1(s_0 - \rho), \tag{22}$$

$$\dot{\epsilon}_{\rho\rho} = -d_1s_0, \tag{23}$$

$$\dot{\epsilon}_{\varphi\varphi} = -\pi \left(\frac{u}{t} + 2d_1\right) + \frac{\pi d_1s_0 + d_1(s_0 - \rho)}{\rho}. \tag{24}$$

3.4 Upper-bound solution

3.4.1 Power dissipation of deformation (\dot{E}_P)

$$\dot{E}_P = \int_V \bar{\sigma} \dot{\epsilon} dV. \tag{25}$$

3.4.2 Power dissipation of friction (\dot{E}_f)

$$\dot{E}_f = \int_A \frac{m\bar{\sigma}}{\sqrt{3}} \Delta V dA. \tag{26}$$

3.4.3 Power dissipation of shear (\dot{E}_S)

$$\dot{E}_S = \int_S \frac{\bar{\sigma}}{\sqrt{3}} \Delta V dS. \tag{27}$$

The relative average forging load (P_{av}) is approximately given by:

$$\frac{P_{av}}{\bar{\sigma}} = \frac{\dot{E}_P + \dot{E}_f + \dot{E}_S}{AV_0\bar{\sigma}}, \tag{28}$$

Parameters used in these formulas are defined as the following:

t	Thickness of the billet;
z	Axial displacement of the punch;
d_1	An undetermined constant;
N	Number of teeth in the sprocket;
u	Unit flow velocity of the upper die;
$\dot{\epsilon}_v$	Total strain rate of volume;
$R_i, R_m, R_f, R_b, R_s, s, s_0$	Distance from the sprocket center to the free surface of billet;
$R(t)$	Distance from the sprocket center to the free surface where the thickness of the billet is t ;
$U_z, U_r, U_\theta, U_\rho, U_\varphi$	Velocities of axial, radial, circumferential directions, and in the direction of p and φ ;
$\dot{\epsilon}_{zz}, \dot{\epsilon}_{RR}, \dot{\epsilon}_{\theta\theta}, \dot{\epsilon}_{\rho\rho}, \dot{\epsilon}_{\varphi\varphi}$	Strain rate in the axial, radial, circumferential direction, and in the direction of p and φ ;
r_f	Fillet radius of the tooth groove circle for the sprocket;
$\alpha, \theta_d, \theta_f, \varphi_0$	Angles in the radius;
$\theta(t), \varphi(t)$	Radius of free surface;
r, p	Radial distance from the coordinate origins;

A	Cross-section of the billet;
V_0	Upper die velocity;
m	Frication factor.

4 Finite element analysis

Based on the implicit Lagrangian FE code (Chandrasekhar and Singh 2011), the commercial FEM package DEFORM-3D V6.1 was applied to simulate the velocity field of cold semi-precision forging. Three-dimensional solid models were established using Pro/E 4.0 software, which were assembled and imported into the DEFORM-3D software in the form of STL files. Tetrahedral elements were used to mesh the grid number of 10,000 and the complete cold forging simulation was performed in 120 steps with displacements for the movement of the top die in each step of 0.15 mm. The velocities of the top die and floating bottom die were consistent at 15 mm/s by setting the processing of the velocity interface in the DEFORM-3D software. The 3D FE model of the cold semi-precision forging operation was constructed as shown in Fig. 5.

5 Experimental work

The cold semi-precision forging experiments for the multi-row sprocket were conducted using 5052 aluminum alloy. A constrained shunt of the core shaft for the hollow billet was applied to ensure the die cavity fully filled. The standard geometry sizes of the bottom die were cut using a wire EDM machine. The die components (die insert, upper die, bottom die and ejector) were produced from hot-work tool steel AISI H13. Generally, there were two alternative bottom dies to choose (the fixed bottom die and the floating bottom die). The main difference between these two

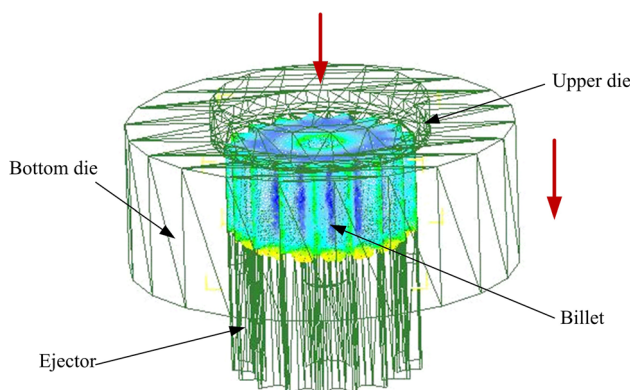


Fig. 5 FEM of the multi-row sprocket in cold semi-precision forging

bottom dies was in the effects of frictional forces in the interface between the billet and the bottom die (Dean 2000; Cai et al. 2004). In design, the bottom die was fixed rigidly to the die holder, and did not move together with the upper die, which gave rise to a resistance from the frictional force. Conversely in the design of the floating bottom die, the upper and bottom dies moved together under the action of a spring, which caused the frictional force to be an effective forging force. The die structure for cold semi-precision forging of the multi-row sprocket was designed as shown in Fig. 6.

A 500 ton hydraulic press was used to forge the sprocket at room temperature. Cylindrical hollow billets, whose initial geometry size was $\phi 60 \times \phi 18 \times 52$ and initial test temperature was 20 °C, were lubricated with oil-base graphite. The velocity controller of the hydraulic press was set to fix the forming velocity of the hydraulic press at 15 mm/s. The displacement of the upper die was measured with a displacement sensor and the load on the hydraulic press was obtained with a load sensor.

6 Results and discussion

6.1 Simulation results

Based on the analysis of the upper-bound method, the velocity field for the cold semi-precision forging process for a multi-row sprocket was verified by FE simulation to

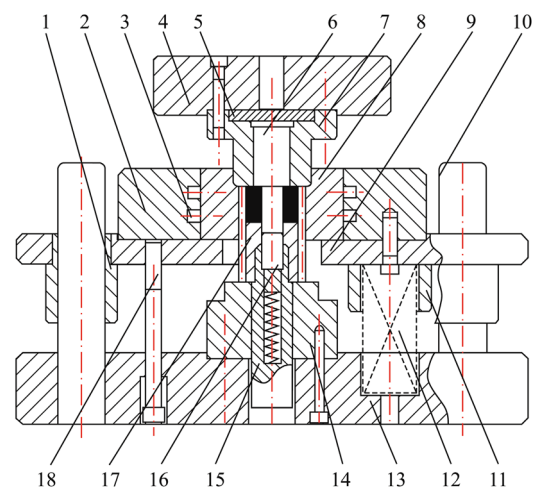


Fig. 6 Schematic of the die structure of a multi-row sprocket in cold semi-precision forging: 1 guide bushing; 2 loading die holder; 3 heating resistor; 4 upper platen; 5 support plate; 6 upper die; 7 upper die holder; 8 floating bottom die; 9 floating die holder; 10 guide pin; 11 spring retainer; 12 spring; 13 lower platen; 14 cushion block; 15 ejector beam; 16 locating pin; 17 ejector of sprocket; 18 hexagon socket head cap screws

obtain the distributions of the velocity fields in the die cavity filling. Figure 7 indicates the distribution of the velocity field of the hollow billet. The maximum velocity

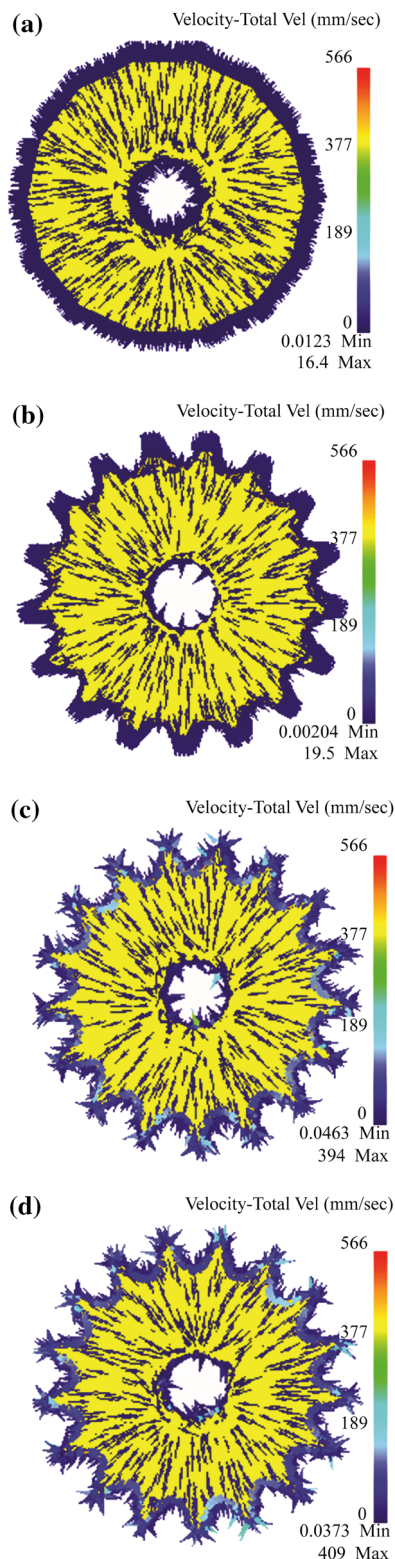


Fig. 7 Distribution of the velocity field at different steps during the cold forging process **a** 34th step; **b** 64th step; **c** 84th step; **d** 104th step

in region ⑤ was 321 mm/s and the minimum velocity in region ① was close to zero (Fig. 8). The fluid particles of the billet were given priority to flow radially and convex ears of the velocity outside the hollow billet occurred when filling the die cavity (Fig. 7b, c, d). The flow velocity of the billet increased sharply in the tooth-groove of the die cavity because of the path with least resistance when the billet made first contact with the die cavity. Because the velocity increased exponentially, the billet fluids fully filled the die cavity. The self-locking of the billet in filling the die cavity resulted in a sharp decrease in the velocity. At the end of the forging stage, irregular fluctuation of the billet fluids occurred in the teeth of the sprocket, as observed in Fig. 7d.

The distribution of the effective stress field reflected the filling resistance and stress concentrations of the deformation billet (Bennett 2013; Wang et al. 2011). Figure 9 shows the distribution of the effective stress field at various steps. As the upper die travel increased, it was obvious that the billet compressed axially and bulged radially. The maximum stress of 213 MPa was found in the teeth of the sprocket billet and higher stress concentrations were indicated at the edges and in the shunt hollows of the billets. A minimum stress of 26.3 MPa was observed in the middle of the sprocket billet. At the end of the forging stage, the restraint effect of the dies reached a maximum, which made the billet flow more difficultly. Larger rough selvages occurred at the bottom of the billet corner. Figure 10 illustrates the variation in effective stress at various steps. It was observed that the effective stress increased exponentially in the initial stage and then remained constant at the end of forging. The value of effective stress in region ⑤ remained the highest at 213 MPa, while region ① remained the smallest. The highest effective stress values were recorded for the teeth of the sprocket because of the severe plastic deformation (SPD). The effective stress of the sprocket decreased from the teeth to the middle of the billet and increased from the middle to the shunt hollows of the sprocket billet.

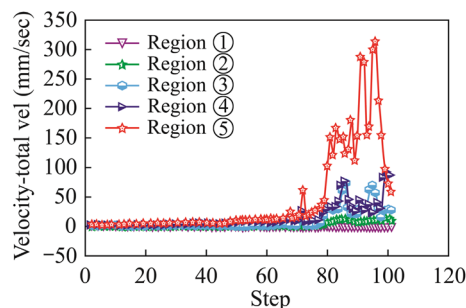


Fig. 8 Variation in velocity at various steps in various deformation regions

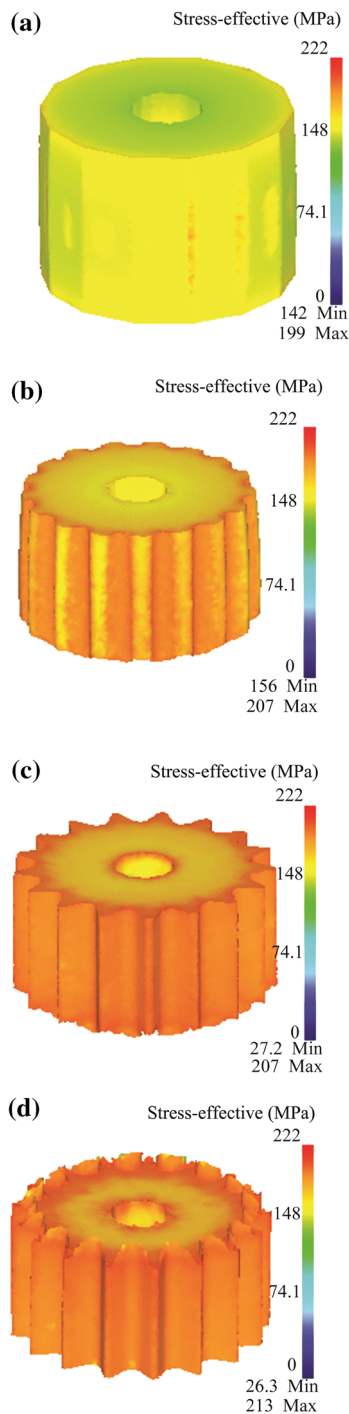


Fig. 9 Effective stress distribution with various steps **a** 34th step; **b** 64th step; **c** 84th step; **d** 104th step

6.2 Experimental results

The simulation results for the forging process provided significant guidance to the practical experiments. It was found that the tooth profile of the forged sprocket in the experiment (Fig. 11) was fully filled and the geometries

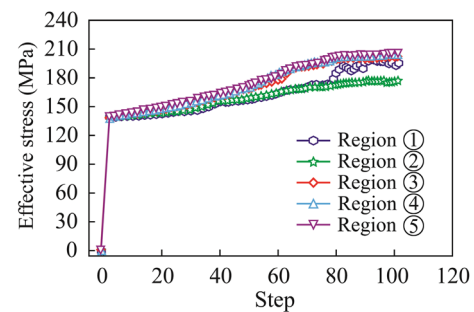


Fig. 10 Variation in effective stress with various steps

of a forged sprocket with the new process possessed good integrity. The similarity in the tooth profile between the experimental and simulated results was obvious. It showed that the results with the new forging process completely fulfilled the engineering requirements in precision forging a multi-row sprocket.

6.3 Forging loads

It was inferred that the velocity discontinuity of the billet was an important factor to take into account in terms of the required forging load. This was extremely significant for designing accurate dies, choosing reasonable equipment and determining a proper process (Can and Misirli 2008; Liu and Cui 2009). The calculated, experimental and simulated load-stroke curves during cold semi-precision forging are illustrated in Fig. 12. It was observed that their variation trends were basically the same and the forging loads increased abruptly owing to the forming of sprocket teeth. The maximum forging load for the experiment was 3399.9 kN, which was less than the equipment load capacity of 5000 kN, while the maximum load calculated with the upper-bound method was 3700 kN and simulated was 3335.8 kN. The relative average forging load obtained using the upper-bound method was greater than from the experimental and simulated results because of the complex boundary conditions, shear loss, friction resistance and deformation energy, etc. The experimental loads were greater than the simulated loads because of the complicated experimental conditions, such as temperature control, friction effect, lubrication, and equipment, which the simulated results did not fully consider. The whole forging process was divided into four stages: free upsetting, filling, corner filling and recovery. The load was relatively lower in the free upsetting stage. In the filling and corner filling stages, the load increased abruptly with the increase in the stroke movement. Finally, the load tended to be stable in the recovery stage. The experimental results were in accordance with the calculated and simulated results, providing a level of validation for the accuracy of the theoretical results.

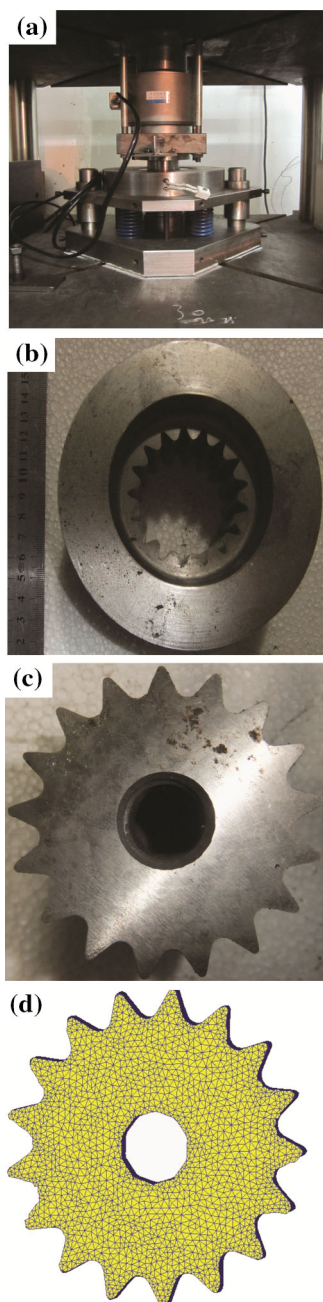


Fig. 11 Photos of the experimental dies and forged sprockets **a** die structure with load sensor; **b** bottom die; **c** forged part; **d** simulated part

7 Conclusions

- (1) The cold semi-precision forging process for a multi-row sprocket and a kinematically admissible velocity field for filling the die cavity were presented and verified to be simple and feasible in practical application.
- (2) The validation of the upper-bound method was undertaken by comparing its results with FEM

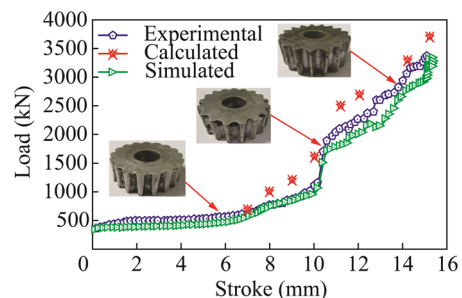


Fig. 12 Load-stroke curves during cold forging of multi-row sprocket

results. The velocity and effective stress fields were obtained and indicated that the upper-bound and FE methods were suitable for analyzing complex three-dimensional plastic deformation.

- (3) The cold forging experiments of the multi-row sprocket were successfully carried out at room temperature. The experimental load-stroke curves were basically in accordance with the calculated and simulated results. This study provides a theoretical foundation for research on the precision forging of a multi-row sprocket.

Acknowledgments This research was financially supported by the National Science Foundation of China (Grant Nos. 51175363 and 51274149).

Open Access This article is distributed under the terms of the Creative Commons Attribution 4.0 International License (<http://creativecommons.org/licenses/by/4.0/>), which permits unrestricted use, distribution, and reproduction in any medium, provided you give appropriate credit to the original author(s) and the source, provide a link to the Creative Commons license, and indicate if changes were made.

References

- Bennett CJ (2013) A comparison of material models for the numerical simulation of spike-forging of a CrMoV alloy steel. *Comput Mater Sci* 70:114–122
- Cai J, Dean TA, Hu ZM (2004) Alternative die designs in net-shape forging of gears. *J Mater Process Technol* 150:48–55
- Can Y, Misirli C (2008) Analysis of spur gear forms with tapered tooth profile. *Mater Des* 29:829–838
- Chandrasekhar P, Singh S (2011) Investigation of dynamic effects during cold upset-forging of sintered aluminium truncated conical preforms. *J Mater Process Technol* 211:1285–1295
- Choi JC, Choi Y (1998) A study on the forging of external spur gears: upper-bound analyses and experiments. *Int J Mach Tool Manuf* 38:1193–1208
- Choi J, Cho HY, Jo CY (2000) An upper-bound analysis for the forging of spur gears. *J Mater Process Technol* 104:67–73
- Dean TA (2000) The net-shape forming of gears. *Mater Des* 21:271–278

- Ghassemali E, Tan MJ, Jarfors AEW, Lim SCV (2013) Optimization of axisymmetric open-die micro-forging/extrusion processes: an upper bound approach. *Int J Mech Sci* 71:58–67
- Jiao HZ, Yang ZJ, Wang SP (2014) Contact dynamics simulation analysis for sprocket transmission system of scraper conveyor. *J Chin Coal Soc* 39(1):166–171 **(In Chinese with English abstract)**
- Kwan CT (2002) An analysis of the closed-die forging of a general non-axisymmetric shape by the upper-bound elemental technique. *J Mater Process Technol* 123:197–202
- Liu J, Cui ZS (2009) Hot forging process design and parameters determination of magnesium alloy AZ31B spur bevel gear. *J Mater Process Technol* 209:5871–5880
- Politis DJ, Lin J, Dean TA, Balint DS (2014) An investigation into the forging of Bi-metal gears. *J Mater Process Technol* 214:2248–2260
- Takagi M, Suganaga K, Nagata T (2009) New PM sprocket meets auto cost, performance concerns. *Met Powd Rep* 64:25–29
- Thipprakmas S (2011) Improving wear resistance of sprocket parts using a fine-blanking process. *Wear* 271:2396–2401
- Wang JH, Chen FX, Deng XZ (2011) Numerical simulation of hypoid driving gear precision forging. *Forg Stam Technol* 36:149–154 **(In Chinese with English abstract)**
- Wang SP, Yang ZJ, Wang XW (2012) Wear of driving sprocket for scraper convoy and mechanical behaviors at meshing progress. *J Chin Coal Soc* 37(2):494–498 **(In Chinese with English abstract)**
- Wu ZM, Wang HY (1992) An upper-bound analysis of shunt forming of gears. *Corp Plast Pro Tech* 23:306–310
- Wu YJ, Dong XH, Yu Q (2014) An upper bound solution of axial metal flow in cold radial forging process of rods. *Int J Mech Sci* 85:120–129
- Yang SH, Fu PF, Huang LJ (1999) Upper-bound model establishment and analysis of cold precision forging of spur gears. *J Jilin Univ Technol* 29:23–28
- Zhao RH, Chi CZ, Wei CJ, Cheng WJ, Liang W (2014) Semi-precision hot forging blocking and die design of multi-row chain wheel. *Forg Stam Technol* 36(6):20–23 **(In Chinese with English abstract)**